CrystEngComm

Accepted Manuscript

ROYAL SOCIETY OF CHEMISTRY

www.rsc.org/crystengcomm

Charged Nanoparticles Crystalizing and Controlling Crystallization: from Coatings, to Nanoparticle Surfactants, to Chemical Amplifiers.

Bartosz A. Grzybowski[1,2]*

[1]Department of Chemical and Biological Engineering and [2]Department of Chemistry

Northwestern University, 2145 Sheridan Rd., Evanston, IL 60208, USA

*Correspondence to: grzybor@northwestern.edu

Abstract: Metal nanoparticles functionalized with self-assembled monolayers of ligands terminated in charged groups constitute a unique class of nanoscopic polyions – or "nanoions" in short – capable of assembling into higher-order structures ranging from two-dimensional coatings on various types of surfaces (including chemically inert polymers as well as inorganic microcrystals) to three dimensional nanoparticle crystals. These crystals can comprise either spherical or non-spherical nanoparticles, can feature unusual particle arrangements (e.g., diamond-like), and – after already being assembled – can be further "post-processed" to act as chemical sensors of unmatched sensitivity. This "post-processing" of the crystals involves functionalization with dithiols that bridge nearby particles but are cleavable in the presence of either small-molecule or enzyme analytes. When the dithiols are cut, the NP crystals disintegrate into tens of millions of brightly colored individual particles translating the presence of few analyte molecules into a macroscopic color change readily detectable to a naked eye. Demonstrations such as this one illustrate what we believe should be the future of nanoscale

assembly – namely, synthesis of structures in which nanoscopic components enable new and useful functions.

1. Introduction.

Nanoparticles and nanoparticle assemblies display a range of properties that are not observed at molecular or colloidal scales. Metal nanoparticles have colors not seen in the corresponding bulk metal states,[1] semiconductor nanoparticles fluoresce,[2] catalytic metals expose high-index crystal planes and show increased catalytic properties,[3] and the assemblies of nanoparticles exhibit unusual electric,[4] optical,[5] magnetic,[6] and mechanical[7] properties. One of the very useful characteristics of nanoparticulate objects is that they allow for versatile engineering of surface characteristics, via the formation of on-particle monolayers of organic ligands.[8] These surface properties can then dictate the assembly of individual nanoobjects into higher-order structures.

Several years ago, our group has initiated research on nanoparticles covered with organic ligands terminated in charged functional groups. This work has led to the discovery of several fundamental nanocale phenomena that set the charged nanoparticles distinctly apart from either molecular ions or colloidal charged particles – to emphasize these differences, we have christened these nanoobjects "nanoions". In this article, we first review these fundamentals of individual "nanoions" but then extend our discussion to self-assembly of several classes of materials comprising nanoionic particles. These materials are rich both in terms of form and function, and include two dimensional as well as three dimensional structures. The former include coatings in which oppositely charged nanoions deposit in a cooperative fashion on various metals, glasses, or polymers, including polymers that are typically considered chemically

inert. In an extension of this cooperative deposition process, the particles control the growth of inorganic microcrystals, effectively acting as nanoparticulate surfactants. In three dimensions, like-charged or oppositely-charged nanoions form crystalline assemblies characterized by either close or open (e.g., diamond-like) nanoparticle packings, and with crystal sizes adjustable by the relative concentrations of positively and negatively charged nanoparticles used. These crystals are unique for one more reason – namely, they can be post-processed in the sense that it is possible to exchange the NP ligands while leaving the crystals intact. Post-processing with dithiols bridging nearby particles within the crystals opens a whole new range of possibilities for engineering and controlling the properties of our assemblies. First, the crystals can become stable in solvents in which they would normally disintegrate. Second, when the dithiols incorporate units that can be chemically or enzymatically cleaved, it is possible to use these constructs as chemical sensors of unprecedented sensitivity. In the examples we illustrate, extremely small quantities of analyte molecules present in solution can cut enough dithiols to "pinch" small holes in the NP crystals to liberate tens of millions of individual, brightly colored "nanoions" into solution. In this way, NP crystals act as chemical sensors amplifying small analyte concentrations into pronounced color changes visible to a naked eye. Third, the "reinforcement" of crystals with dithiols enables using them as seeds for further growth leading to layered "crystals-within-crystals". Together, these capabilities not only extend the repertoire of NP self-assembly approaches but, above all, define a new level of usefulness of these superstructures. While many other types of NP crystals have been studied – notably, the ones covered with DNA strands[9] – the focus of these works has been on the structure of the crystals and their relevance to the fundamentals of self-assembly. Having witnessed and participated in the explosion of the self-assembly research over the last two decades, the author of this paper feels that synthesis of

more nanopartculate assemblies is, per se, not a very fruitful avenue of future research. Instead, the time is ripe to demonstrate that these assemblies have practical uses – else, the field will sooner or later saturate with a plethora of structures that are interesting for the aesthetics of SEM images but irrelevant to the true challenges (e.g., energy harnessing, biological detection) of nanochemistry. The ultimate goal of the current article and of the examples it contains is to stimulate (or even, provoke) thinking along these application-oriented lines.

2. Basic properties of "nanoions". At the heart of our work are well-known metal (Au, Ag, Pd) nanoparticles 3-11 nm in diameter and coated with self-assembled monolayers (SAMs) of ω-functionalized alkane thiols.[8] This system is experimentally convenient because tightly-packed SAMs on noble metals form readily and because electrical charges can be introduced onto the NPs in a straightforward fashion by using thiol ligands terminated in charged groups. In our initial experimental scheme,[10a] we studied solutions of equally sized AuNPs derivatized with either positively charged *N*,*N*,*N*-trimethyl(11-mercaptoundecyl)ammonium chloride (TMA, pK_a > 13) or with negatively charged mercaptoundecanoic acid (MUA, pK_a in NP/SAM ca. 6-8), with the pH of the latter adjusted to 11 to fully deprotonate the carboxylic groups. Once prepared, a stirred solution of NPs (0.2-5 mM) of one polarity was then titrated with small aliquots of a solution (0.2-5 mM) containing oppositely charged NPs (Figure 1a). Remarkably, the solution remained stable until precipitating sharply only when the numbers of the NPs of opposite polarities became equal. Prompted by this observation, we preformed a series of additional experiments,[10b] in which we varied the nanoparticles' relative sizes, surface charges (e.g., by using mixed disulfides with only one "arm" terminated in a charged group), material properties of the metal cores, and the ionic strength of the solutions. In all cases, the mixtures of

NPs exhibited threshold, ion-like (hence, "nanoions") precipitation within ~3% from the theoretically expected point of NP electroneutrality – that is, a point at which the charges on the NPs were compensated, $\sum Q_{NP(+)} + \sum Q_{NP(-)} = 0$.

It is worth emphasizing that this precipitation behavior is fundamentally different from either the molecular or the colloidal regimes. Whereas oppositely charged molecular ions can remain stable in solution until reaching a certain threshold (determined by pertinent equilibrium constants, such as K_{sp}) at which they start to precipitate, oppositely charged microparticles precipitate continuously over a wide range of relative particle concentrations[11] (Figure 1b).

The ζ-potential and dynamic light scattering (DLS) measurements evidenced (Figure 1c) that during titration, the NPs aggregate and the sizes of these aggregates increase rapidly near the precipitation point. At the same time, the surface potential of the mixed NPs is initially constant and equal to that of the "majority" NPs present in solution. When the solution is about to precipitate, however, the magnitude of the potential decreases rapidly and is zero at the precipitation point (Figure 1d). These findings suggest that the NPs form aggregates whose outer shells contributing to surface potential are composed mostly of the "majority" NPs (Figure 2a). These shells render all aggregates like-charged and stabilize them in solution by mutual electrostatic repulsions. When the net charge on the NPs is close to neutral, there are not enough "excess" NPs to form like-charged shells, and precipitation ensues.

Formation of the core-and-shell aggregates is further supported by UV-Vis measurements of mixtures of oppositely-charged NPs having different metal cores and different locations of the optical absorption maxima, λ_{max}. An illustrative example here is the titration of AuNPs with oppositely-charged AgNPs whereby addition of silver particles does not give rise to any Ag SPR band expected at 424 nm but, instead, causes the enhancement of the AuSPR band at 520 nm

(Figure 2b). This phenomenon can be explained on the basis of the classical Mie theory,[5] which predicts that if the impinging light passes through a thin shell of AuNPs before reaching the silver NPs, its wavelength decreases by a factor determined by the shell's effective refractive index. As a result, the AgNPs are resonantly excited at a longer effective wavelength, $\lambda_{eff} = \lambda_{intrinsic} n_{shell}$ ~ 520 nm and the silver SPR band at 424 nm appears "extinguished" while that of gold at ~520 nm, is "enhanced."

Taken together, the experiments indicate that oppositely-charged NPs maintain themselves in solution by using excess NPs of either type to build "protective," like-charged shells around the forming aggregates. At the point of NP electroneutrality, these extra particles run out, and the aggregates precipitate.

3. Interactions between the nanoions and the importance of electrostatic screening. The structural details of the NP aggregates such as those illustrated in Figure 2 merit further discussion. The key question that needs to be addressed is why these aggregates are stable at all – despite having net charge on the constituent NPs. In vacuum, a structure comprising a negatively charged particle surrounded by several positively charged particles would have a very unfavorable electrostatic energy on account of like-charge repulsions. In solution, however, the charges on the NPs are screened by counterions which, as we will see shortly, not only render the electrostatic interactions short ranged but also make their magnitudes dependent on NP polarity, which is a purely nanoscale effect.[12]

To describe the electrostatic interactions between two charged, spherical NPs in ionic solution, it is first necessary to solve for the electrostatic potential, φ, and then derive the free energy of interaction via thermodynamic integration.[13,14] For surface potentials less than ~50

mV, the potential in solution is well approximated by the linearized Poisson-Boltzman (PB) equation, $\nabla^2\varphi = \kappa^2\varphi$, where $\kappa^{-1} = \sqrt{\varepsilon_0 \varepsilon k_B T / 2n_0 e^2}$ is the Debye screening length, n_o is the monovalent salt concentration, e is the fundamental charge, ε_o is permittivity of vacuum, ε is the dielectric constant of the solvent, k_B is Boltzmann's constant, and T is the temperature. The PB equation is solved with the so-called "charge-regulating" boundary condition that accounts for the equilibrium between counterions adsorbed onto the charged NP ligands and those "free" in solution. For the case of an NP coated with N_T positively charged surface ligands, A^+, in a solution containing negatively charged counterions, B^-, this equilibrium is determined by $N_{A+}C_{B-} / N_{AB} = K_+ \exp(e\varphi_s / k_B T)$, where N_{A+} and N_{AB} are, respectively, the numbers of counterion-free and counterion-bound surface ligands ($N_{A+} + N_{AB} = N_T$), C_{B-} is the concentration of counterions in solution, K_+ is the equilibrium constant in the absence of any external fields, and φ_s is the electrostatic potential at the NP's surface. From this relation, the surface charge density, σ, may be expressed as $\sigma = e\rho / [1 + (C_{B-} / K_+)\exp(e\varphi_s / k_B T)]$, where $\rho = N_T / 4\pi R^2$ is the surface density of charged groups, and R is the NP radius. Assuming the dielectric constant of the NPs ($\varepsilon_p \approx 2$ for the SAM coating) is small compared to that of the solvent ($\varepsilon \approx 80$ for water), the surface charge is related to the potential at the NP surface by $\sigma = -\varepsilon_0 \varepsilon \nabla\varphi \cdot \vec{n}$, where $\vec{n}$ is outward surface normal. Equating the two relations for σ provides the necessary boundary condition for a positively charged NP; the case of a negatively charged particle may be derived in similar fashion.

Solving the PB equation for the case of two interacting NPs yields interaction potentials plotted in Figure 3b. The most interesting feature of these dependencies is that the attractive energy between oppositely charged NPs at contact is nearly twice that of like-charged NPs at the

same distance. This effect is due to the desorption of bound ions from the NPs' surfaces in the regions of reduced electrostatic potential (cf. the equilibrium relation above). Specifically, when oppositely charged NPs approach one another, the magnitude of the potential in the region between them decreases (Figure 3a, *left*) causing counterions to desorb. This desorption, in turn, increases the local charge density and the electrostatic interaction energy. In contrast, the magnitude of the potential between proximal, like-charged NPs is enhanced (Figure 3a, *right*), causing further adsorption of counterions, decrease in the local charge density, and reduction of the electrostatic interaction energy. The differences in the like-charged and oppositely-charged interaction potentials are of central importance in rationalizing the nanoionic assemblies – namely, the electrostatic repulsions that would tend to disrupt these assemblies are weaker than the attractive interactions mediating particle self-assembly.

Naturally, one also needs to consider the van der Waals interactions that are always attractive (i.e., irrespective of NP polarity). As discussed in detail in refs[12-15], these interactions for 8 nm particles (5 nm core plus 3 nm SAM thinkness) are only 1-2 kT, meaning that for the particle sizes used, the assembly is dominated by electrostatic interactions; the vdW attractions becomes dominant only for particles of radii $R > \sim 35$ nm.

NVT Monte Carlo simulations based on these considerations help understand the precipitation behavior at the point of electroneutrality. This is illustrated in Figure 3d which plots the ratios of positive to negative particles present in solution, $\chi = NP(+)/NP(-)$, against the sizes of the forming aggregates, D. As seen, D scales as $(0.5 - \chi)^{-1}$, which diverges at electroneutrality, $\chi = 0.5$ (Figure 3d).

.

4. Electrostatic self-assembly on surfaces. As we have seen, electrostatic interactions can mediate aggregation of nanoionic particles. In this and subsequent sections, we will review the types of structures and materials these aggregation processes give rise to. We begin the discussion with nanoparticulate surface coatings which – though not having long-range crystalline order – are amongst the most important nanostructured materials and can also control crystallization of other substances.

4.1. Nanoparticulate surface coatings. Depending on the nature of their components, nanoparticle-based coatings can exhibit a range of useful properties including electronic, optical,[16] mechanical,[17] and biological.[18] Electrostatics-based assembly of charged NPs provides a facile route to the formation of coatings whose unique feature is that they form on a variety of materials including glasses, semiconductors, or polymers (including "inert" ones such as polypropylene) without the need for chemical/covalent ligations. In our method (described in [19]), the coatings are deposited from solutions containing the by-now familiar oppositely charged NPs – while stable in dilute solution, these NPs adsorb onto any surface presenting residual charge developed via spontaneous oxidation in air or by plasma treatment. Interestingly, adsorption is cooperative[20] in the sense that it requires the presence of particles of opposite polarities (like-charged NPs adsorb only marginally due to interparticle repulsions). The NPs initially "seed" the surface slowly, but as the adsorption progresses, its rate accelerates before finally leveling off when the surface becomes crowded; overall, adsorption kinetics is sigmoidal. Qualitatively, the cooperativity in this system is due to the fact that the +/- NPs already present on the surface facilitate attachment of even more particles, much in the same way as a "seed" of an ionic crystal promotes further crystal growth. An interesting feature of the NP adsorption mechanism is that the process self-terminates after the deposition of exactly a monolayer of nanoparticles. This

monolayer comprises equal numbers of positively and negatively charged NPs and thus presents no net charge that could facilitate attachment of more NPs. On the other hand, when the deposited monolayer is washed with base (to deprotonate some of the ligands on the NPs), it regains its net charge and ability to promote further NP adsorption – in this way, multilayered NP coatings can be deposited.

Referring a reader interested in the mechanistic/theoretical details to references [19,20] we highlight some practical advantages of the method. First, since deposition leads to monolayers incorporating equal numbers of "+" and "–" NPs and is driven by the electrostatics alone (and not by the nature of the NPs' cores), it is possible to prepare the coatings made of different combinations of materials. For example, a solution of 25% of AuTMA NPs, 25% of AgTMA NPs and 50% of PdMUA NPs (TMA = SH-$(CH_2)_{11}$-$N(CH_3)_3^+$; MUA = SH-$(CH_2)_{11}$-COO^-) deposits a coating whose elemental composition is 1:1:2 (see Figure 4a for this and other examples). Second, because deposition is solution based, it can give uniform coatings over curved surfaces, including inner surfaces of vials and tubing[21]. Figure 4b shows examples of AgNP(+)/AgNP(-) coatings formed inside of Tygon tubing used in medical applications – owing to the bacteriostatic nature of silver nanoparticles, the tubing remains sterile in the presence of both Gram positive *S. Aureus* and Gram negative *E. Coli* bacteria. Finally, the ordering of the coatings can be improved by performing the deposition in the presence of AC fields that "jiggle" the charged particles and drive their close packing (Figure 4c). The electrohydrodynamic phenomena accompanying AC forcing are described in detail in our publication.[22]

4.2. Nanoionic coatings controlling the growth of microcrystals. Since the nanoionic coatings form on a wide variety of surfaces, we have also examined[23] a situation where their deposition would compete with the growth of other (inorganic or organic) microcrystals present

in the same solution. Although the growth of microcrystals can be controlled by various agents (e.g., multivalent ions,[24a] charged small molecules, [24b] mixed cationic-anionic surfactants, [24c] polyelectrolytes[24d] and other polymers,[24e] micropatterned self-assembled monolayers,[24f] proteins,[24g] and also biological organisms during biomineralization[24h]) the chief limitation of current approaches is that the growth-modifying agents are typically specific to the crystalizing material. In contrast, oppositely-charged nanoions can function as universal "surfactants" that control the growth and stability of microcrystals of monovalent or multivalent inorganic salts, and of charged organic molecules. Several examples are shown in Figure 5.

Mechanistically, the process can be described by a crystallization-NP deposition mechanism in which the (+) and (–) NPs adsorb non-specifically onto the surfaces of the growing crystals to physically retard their growth. In this process, the kinetics of crystal growth competes with that of NP monolayer formation. As NPs gradually adsorb in time onto the crystal surface, the rate of crystal growth decreases – consequently, an increase in NP concentration results in faster NP adsorption, slower crystal growth, and thereby smaller crystals upon formation of a complete NP monolayer. Interestingly, by making the reasonable assumptions that (i) NP adsorption onto the microcrystals is described by a Langmuir-type kinetic model and (ii) the rate of crystal growth is proportional to the free crystal surface area, the proposed mechanism reproduces the experimentally observed inverse scaling of the crystal size, d, with the ratio of the concentration of the NPs to the concentration of the salt, $d \sim 1/\chi$, where χ C_{NP}/C_{salt}.

Another interesting aspect is the polyvalent nature of the crystal-NP interactions. In general, the interactions between the adsorbate and the crystal surface must be sufficiently strong to yield an overall favorable/negative free energy of adsorption. For small-molecule growth

inhibitors, strong binding requires rather precise molecular recognition of a particular crystal surface; consequently, these inhibitors are not universally effective. In case of our NPs, similar binding affinities are achieved through many non-specific interactions acting in concert, resulting in the ability of these particles to adsorb strongly onto a variety of different surfaces. In addition to polyvalent interactions between charged ligands bound to the NPs and the crystal surface, the charged nanoparticles we use benefit further from the (+)/(–) interparticle interactions, which further facilitate non-specific adsorption.

5. 3D nanoparticle crystals. So far, we have described electrostatic assembly schemes that require the presence of a deposition substrate. Naturally, it would be desirable to extend these schemes to three-dimensional nanomaterials. However, the task of organizing charged NPs into 3D crystals is not a trivial one, since the relatively strong electrostatic forces often lead to flocculation and rapid precipitation rather than crystallization. The key to successful crystallization is, as with molecular ions, to make the process very slow. In a class of systems our group developed[25], oppositely charged ~ 5 nm NPs are crystallized from a mixture of water and DMSO. When the "good" solvent (water) is slowly being evaporated at 65 ^{o}C, the NPs become less readily soluble and assemble into sharply-faceted crystals, each comprising several millions of nanoparticles (Figure 6). While for equally sized and oppositely charged NPs one might expect – by analogy to inorganic ions – the crystal structure to be either NaCl or CsCl, nanoscale electrostatics again defies the intuitive. Surprisingly, the NPs crystallize into diamond-like structure, in which each NP is surrounded by four tetrahedrally arranged neighbors. Although in the diamond lattice each NP forms only $n = 4$ favorable "+/-" contacts (versus $n = 6$ in NaCl and $n = 8$ in CsCl), the like-charged particles in this open-lattice structure are farther apart than in the

closed-packed NaCl or CsCl. We have seen in Section 3 that this effect can be attributed to the screening by the surrounding counterions and due to charge regulation which weakens like-charge repulsions compared to opposite-charge attractions; because the screening length around the NPs is commensurate with the particle diameters, the repulsions between like-charged, next-nearest-neighbors in the diamond lattice are screened and effectively do not contribute to the unfavorable electrostatic energy of the crystal. Colloquially put, by "opening up" the structure one loses the favorable "+/-" energy, but saves on the "+/+" and "-/-" unfavorable contributions.

Also, we have recently performed rigorous free energy calculations and showed[26] that while screening is an important factor, the formation of diamond-like nanoionic crystals is further facilitated by a slight charge imbalance between the (+) and (–) nanoparticles – an effect that is indeed observed in experiments with Au and Ag NPs differing in size by a fraction of a nm and co-crystallizing more readily than perfectly monodisperse NPs (see [25a]). This size difference translates into the ratio of particles' charges deviating from minus unity ($\sigma_- / \sigma_+ \neq -1$) with the excess charge, $\Delta\sigma = \sigma_+ + \sigma_-$ on the NPs balanced by counterions within the unit cell to maintain overall charge neutrality. For this situation, our calculations of counterion distributions and of the free-energy over unit cells of various possible 1:1 lattices (ZnS, NaCl, CsCl) demonstrated that for *any* amount of excess charge $\Delta\sigma$, ZnS is thermodynamically favored over CsCl or NaCl structures. These considerations illustrate an intriguing point – while in molecular crystal engineering one typically strives to "match" the interactions between co-crystallizing species as closely as possible, at the nanoscale a certain degree of imperfection and polydispersity can actually be beneficial and can help the system to select certain structures that would otherwise not be observed.

We also note that akin to nanoionic NPs controlling the sizes of microcrystals made of different substances (cf. Section 4.2), these particles can "self-regulate" the sizes of crystals growing from mixtures of (+) and (–) nanoions themselves. This is illustrated in Figure 7 which shows nanoionic crystals differing in size from several tens of nanometers up to several microns[25b]); the control parameter here is the excess, ε, of NPs of either polarity. The measurements of the ζ- potential indicate that these excess NPs "terminate" crystal growth by forming protective shells around the growing assemblies – although the particles in these shells are all like-charged, the interactions between them are effectively screened, and the shells are stable.

6. Nanoionic crystals as chemical amplifiers. Three-dimensional crystals made of charged nanoparticles we have seen in the previous Section are soluble in water. When, however, these crystals are placed in a solution of dithiol molecules, HS-$(CH_2)_n$-SH, the thiol groups covalently crosslink the nearby particles near the crystals' surfaces and thus make these crystals stable in aqueous media. The crystals reinforced in this way offer some exciting opportunities for engineering *functional* nanostructured materials.

In particular, when stabilized by analyte-specific cross-linkers (dithiols with groups prone to cleavage upon reaction with analyte molecules) such crystals are still stable in pure water, but rapidly dissolve when specific molecules are present in solution (see reference [27] and Figure 8). Each of such crystals can be depicted as having a thin "reinforced" skin (composed of few layers of NPs cross-linked on the crystal's surface), while the vast majority of NPs inside it remain uncrosslinked and thus water soluble. Upon addition of a specific analyte which "cuts" the cross-linkers, millions of individual NPs from inside of the crystal are liberated. These NPs adsorbing

strongly in the visible regime give rise to a pronounced color change, easily observed with a naked eye (Figure 9). The most important feature of this system is the amplification of the disassembly process – as we will see shortly, only few molecules of analyte are needed to "cut" several "holes" in the crystal's "skin" in order to liberate several millions of nanoparticles.

In our studies, we considered various cleavable dithiols stabilizing the crystals including: for instance, (**1**) 11-mercaptoundecyl 11-mercaptoundecanoate containing an ester moiety prone to base hydrolysis; and (**2**) N-(6-amino-1-(11-mercaptoundecylamino)-1-oxohexan-2-yl)-11-mercaptoundecanamide incorporating a lysine amino acid and cleaving in the presence of proteases such as Trypsin or Proteinase K (but not Papain; see Figure 8a for structures). Irrespective of the crosslinker's structure, the stability of NP crystals in water increased with increasing dithiol concentration. On the other hand, if too much dithiol was used, the "tightly-knit" crystals were hard to dissolve upon exposure to dithiol-cutting analytes, and the sensitivity of detection was poor. Consequently, the crystals we used were crosslinked with the minimal concentration of dithiols (~ 2 mM, 6-8 hrs of soaking) necessary to stabilize these crystals.

When an analyte specific to cleavable dithiols was added, the crystals dissolved coloring the solution brightly (Fig. 9a). SEM imaging (Fig. 9b) indicated that crystals dissolved from one or few locations on their surfaces. These locations were usually along crystal's edges or near its vertices, where the surface NPs were the least stable (i.e., corresponding to the highest free-energies). Once a small hole was "pinched" in the crystal's crosslinked "skin," large numbers of individual NPs spilled from the crystal's interior into the solution. DLS measurements in Figure 9c (*black and red histograms*) confirmed that this process – even for the lowest analyte concentrations used – gave mostly individual NPs rather than nanoparticle clusters in solution. This behavior was in sharp contrast to that observed in control experiments, where we studied

the dissolution of crosslinked but disordered NP aggregates (Figure 9c, *violet and gray histograms*). Such aggregates not only required much higher concentration of dithiols to be stable in water (>> 10 mM), but also dissolved slowly and gradually – first into smaller, colorless aggregates and only then into individual NPs. As a result, the sensitivity of detection was much lower upon the dissolution of disordered aggregates than of NP crystals.

Quantification of these trends by measuring the changes in solution's absorbance (proportional to the concentration of dissolved NPs) upon addition of analyte molecules evidenced that this absorbance was at least 100 times higher during dissolution of crystals than of disordered NP aggregates – in other words, crosslinked crystals offered at least two-orders-of-magnitude improvement in sensitivity. The dissolution of crystals was also much more rapid – a typical crystal sample (ca. 8.8×10^7 crystals or 2.2×10^{14} NPs in 4 mL of solvent) exposed to an analyte of concentration ~ 1 μM dissolved completely within 60 sec; for a disordered NP aggregate exposed to a tenfold higher analyte concentration, the time to see even a bleak color were on the order of tens of minutes. Lastly but not least, for the crystals, the smallest change in the solution's color discernible to a naked eye (*Abs* ~ 0.3 – 0.4 in a 10 mm cuvette) was observed upon addition of only few tens of analyte molecules, which compares very favorably to conventional NP-based colorimetric methods requiring approximately 1,000 or more analyte/small molecules to effect even minute spectral shifts/changes detectable using spectroscopic methods.

Similarly, crystals stabilized with dithiols containing enzyme-specific motifs acted as selective enzymatic sensors. For instance, crystals crosslinked with lysine-containing dithiol **2** were dissolved readily by ~ 5 μM solutions of serine proteases such as trypsin or proteinase K, whose active centers contain the serine-histidine-aspartate catalytic triad. The smallest detectable

change in the solution color detectable by a naked eye corresponded to 56 molecules of trypsin or proteinase K per one liberated nanoparticle. In contrast, the same crystals remained stable in the presence of even high, > 0.1 mM, concentrations of protease papain, whose catalytic triad is cysteine-histidine-asparagine and has low affinity to **2**.

7. **"Russian doll" NP crystals.** As mentioned, crystals stabilized with dithiol linkers become stable in aqueous media in which they were originally grown. This property allows re-using such crystals as seeds for the deposition of additional nanoionic particles to ultimately yield multi-layered, "Russian doll" crystals (Figure 10) useful in additional modes of amplified sensing. Specifically, when the "core" and the "shell" regions are made of different NPs and are stabilized by crosslinks specific to different analytes, it is possible to dissolve the core and the shell selectively, and liberate the NPs that make these regions sequentially. While in homogeneous solutions such sequential sensing is probably of little advantage (one can always use two types of "regular" crystals, each stabilized with different crosslinks), it can be of use in "stratified" media where different regions contain different types of analytes. This is illustrated in Fig. 10 for core-and-shell crystals comprising Au cores stabilized with crosslinks **2** and Au/Ag shells stabilized with **1**. When these crystals are first exposed to a medium containing OH^- analyte (cutting the "outer" **1** crosslinks), the shell dissolves; subsequent passage through a medium containing proteinase K (cutting "inner" **2** crosslinks) dissolves the crystal's core. Importantly, when the same crystals are passed through the same media but in reverse order, only shells dissolve but the cores remain intact. In other words, the crystals perform spatially distributed sensing, whereby they report the "path" they travelled (we emphasize that this cannot be achieved with mixtures of "regular" crystals of different types/crosslinks). This property can be even more relevant to

nanoparticle based delivery systems, whereby appropriately structured and crosslinked "Russian doll" crystals travelling through chemically stratified media release their cargo sequentially in desired locations. An exciting opportunity for future research here is to use crystals of medically relevant nanoparticles (e.g., antibacterial AgNPs, antifungal CuNPs, anticancer arsenic NPs, MRI contrast-enhancing magnetite NPs) in biodelivery applications, where the crystals could dissolve and liberate/disperse their contents sequentially upon reaching specific locations within a body (e.g., low-pH stomach followed by high-pH intestine) or even within individual cells.

8. Crystals of non-spherical nanoions. All of the crystals discussed so far comprised spherical nanoparticles. This selection reflects the fact that crystallization of non-spherical nanoobjects (rods, plates, etc.) is significantly more difficult and remains an experimental challenge. For such particles, crystallization is often prevented by strong van der Waals (vdW) attractions that lead to indiscriminate aggregation/flocculation of the particles rather than to orientation-specific self-assembly. This is quite limiting since assemblies of nanoobjects of complex shapes could enable additional sensing modalities – in particular, those based on the enhancement of electromagnetic fields around the high-curvature corners of the particles (e.g., Surface Enhanced Raman Specroscopy, SERS[28,29]).

With this in mind, we have extended[30] the electrostatic-based approach to systems comprising metallic nanoplates and in particular nanotriangles, NTs. However, because we wished to weaken the vdW attractions between these objects, we functionalized *all* of them with ligands of one charge polarity – in this way, the repulsive electrostatic interactions partly offset the vdW attractions allowing the particles to fine-tune their mutual orientations and assemble into regular crystals.

In our experiments,[30] the as-prepared NTs were first stabilized by hexadecyltrimethylammonium bromide (CTAB). For these particles, crystallization protocol based on solvent evaporation led to disordered aggregates as illustrated in Figure 11a. When, however, the NTs were functionalized with charged ligands such as N,N,N-trimethyl(11-mercaptoundecyl) ammonium chloride, TMA, they crystallized into large arrays several layers thick (Figure 11b). Furthermore, when the charge on the NTs was further increased by intercalation of charged surfactants into charged SAMs, the triangles formed large-area monolayers (Figure 11c).

We rationalized these observations based on the interplay between van der Waals (vdW) attractions and electrostatic repulsions. Calculations detailed in [30] showed that for the NTs we used, the maximal surface area of contact (when two triangles are stacked perfectly) is ~11,000 nm^2, and the corresponding $E_{vdw} \sim -820\ kT$. On the other hand, for NTs stabilized by CTAB alone, the surface potential was measured at $\varphi_o = 35$ mV, and the calculated energy of electrostatic repulsion is $E_{el} \sim 330\ kT$. Since this energy is significantly smaller than E_{vdw}, the process of assembly is dominated by vdW forces leading to rapid and indiscriminate aggregation. This situation changes for TMA-functionalized NTs for which $\varphi_o = 60$ mV and $E_{el} \sim 960\ kT$ is commensurate with E_{vdw}. In this case, the "balance" between electrostatic repulsions and the vdW attractions allows the NTs to adjust their mutual orientations during assembly leading to well-ordered, multilayer structures. Finally, when TMA SAM has extra charged surfactant intercalated, $\varphi_o = 79$ mV and $E_{el} \sim 2{,}300\ kT$ – then, the net interaction between the NTs is repulsive and the stacking of the NTs into multilayers is energetically unfavorable. At the same time, the triangles are large and massive enough that they sediment from solution onto the deposition substrate where they form monolayers.

In this context of sensing, we capitalized on the enhancement of electromagnetic fields[28,29] between the tips of adjacent triangles within the assemblies. We used confocal Raman spectroscopy to map out these enhancement using small amounts (few μM) of methylene blue (MB) whose C-C ring stretch mode at 1,621 cm^{-1} was previously used to map Raman hotspots of round nano-disks. An optical image in Fig. 12a and confocal Raman map of a MB-laced NT multilayer crystal shown in Fig. 12b illustrate that intense enhancement is observed over the crystal's surface while the surrounding bare Si surface (with identical MB concentration and even with much longer integration times) shows no enhancement. While these observations prove that NT assemblies are SERS-active, they do not *per se* demonstrate that ordering enhances the signal compared to that of the individual NTs. Therefore, to gauge the influence of crystalline ordering on SERS enhancement, additional confocal Raman maps were collected of randomly assembled, CTAB-stabilized NT aggregates with similar NT densities and MB concentrations (Fig. 12c,d). Under these conditions, the intensities of the MB peaks were enhanced compared to regions where no nanotriangles were present but were approximately one order of magnitude less than the intensities of peaks recorded over NT crystals. From these experiments – quantified in the form of Raman spectra such as those in Fig. 12e – we concluded that it is the assembly of NTs into crystals that leads to a significant SERS enhancement. Naturally, these are but a preliminary demonstration and more work is needed to bring this NT system (and others similar to it) to the level of functional, sensing nanomaterials – we are actively working on such extensions.

8. Summary and outlook. In summary, nanoionic particles are unique building blocks from which to assemble a range of nanostructured materials. By adjusting the charges on these

objects, one can modulate the screening length and effectively fine-tune interaction potentials. Unlike molecular ions, the shapes of the nanoions can be almost arbitrary and are limited only by the innovative methods of nanosynthesis which, to date, have produced particles ranging from spherical, through polygonal, to star- or cage-shaped, and many more. Adding charged ligands onto such objects can then drive assembly modes that would be hard (if not impossible) to achieve with only vdW and short-range molecular interactions (vide diamond-like assemblies or nanotriangle lattices). Nanoions are also easy to synthesize and the assembly schemes based on electrostatic forces are experimentally very robust invariably leading to large numbers of well-defined crystals – indeed, in our laboratory, we are nowadays growing NP crystals from up to liters of NP solutions with the (slow) solvent evaporation rate being the only experimental parameter that needs careful monitoring. Other competing methods (e.g., DNA based assembly schemes from the Mirkin's laboratory[9a,b]) are less robust and smaller-scale.

Yet all of these advantages are minutia compared to the main challenge we believe nanoscale self-assembly is facing – namely, whether the assembled materials will have practical applications. And is there any advantage of having NPs packed into crystals rather than simply aggregating them into disordered structures? For ourselves, we have so far identified only one case where nanoparticle crystals are clearly superior to random aggregates – this example is of the chemical amplifiers reinforced with analyte-cleavable dithiol linkers (cf. Sections 6 and 7). It is our great hope that the readers will be able to identify more such applications. Assembling more NP structures for the sake of publishing aesthetic images is not going to define the future of nanoscale self-assembly, if such a future is to exist at all.

References:

(1) N. L. Rosi and C. A. Mirkin, *Chem. Rev.* 2005, **105**, 1547.

(2) A. P. Alivisatos, *Science* 1996, **271**, 933.

(3) Z. R. Tian, W. Tong, J. Y. Wang, N. G. Duan, V. V. Krishnan and S. L. Suib, *Science* 1997, **276**, 926.

(4) W. P. McConnell, J. P. Novak, L. C. Brousseau, R. R. Fuierer, R. C. Tenent and D. L. Feldheim, *J. Phys. Chem. B* 2000, **104**, 8925.

(5) A. M. Kalsin, A. O. Pinchuk, S. K. Smoukov, M. Paszewski, G. C. Schatz and B. A. Grzybowski, *Nano Lett.* 2006, **6**, 1896.

(6) A. H. Lu, E. L. Salabas and F. Schuth, *Angew. Chem. Int. Edit.* 2007, **46**, 1222.

(7) R. Klajn, K. J. M. Bishop, M. Fialkowski, M. Paszewski, C. J. Campbell, T. P. Gray and B. A. Grzybowski, *Science* 2007, **316**, 261.

(8) (a) D. Witt, R. Klajn, P. Barski and B. A. Grzybowski, *Curr. Org. Chem.* 2004, **8**, 1763; (b) J.C. Love, L.A. Estroff, J.K. Kriebel, R.G. Nuzzo and G.M. Whitesides, *Chem. Rev.* 2005, **105**, 1103.

(9) (a) R.J. Macfarlane, M.R. Jones, B. Lee, E. Auyeung and C.A. Mirkin, *Science* 2013, **341**, 1222; (b) E. Auyeung, E. Li, I.N.G. Ting, A.J. Senesi, A.L. Schmucker, B.C. Pals, M.O. de la Cruz and C.A. Mirkin, *Nature* 2014, **505**, 73.

(10) (a) A. M. Kalsin, B. Kowalczyk, S. K. Smoukov, R. Klajn and B. A. Grzybowski, *J. Am. Chem. Soc.* 2006, **128**, 15046; (b) A. Kalsin, B. Kowalczyk, P. Wesson, M. Paszewski and B. A. Grzybowski, *J. Am. Chem. Soc.* 2007, **129**, 6664. (c) K.J.M. Bishop and B.A. Grzybowski *Chem. Phys Chem.* 2007, **8**, 2171.

(11) (a) A. Y. Kim and J. C. Berg, *J. Coll. Int. Sci.* 2000, **229**, 607; (b) J. M. Lopez-Lopez, A. Schmitt, A. Moncho-Jorda and R. Hidalgo-Alvarez, *Soft Matter* 2006, **2**, 1025; (c) P. D. Yates, G. V. Franks, S. Biggs and G. J. Jameson, *Coll. Surf. A* 2005, **255**, 85.

(12) (a) K.J.M. Bishop, C.E. Wilmer, S. Soh and B.A. Grzybowski, *Small* 2009, **5**, 1600; (b) D.A. Walker, B. Kowalczyk, M.O. de la Cruz and B.A. Grzybowski, *Nanoscale* 2011, **3**, 1316; (c) J. N. Israelachvili, *Intermolecular and Surface Forces*, Academic Press, New York **1991**.

(13) S. L. Carnie, D. Y. C. Chan and J. S. Gunning, *Langmuir* 1994, **10**, 2993.

(14) E. J. W. Verwey and J. T. G. Overbeek, *Theory of the Stability of Lyophobic Colloids*, Elsevier, New York **1948**.

(15) V. A. Parsegian, *Van der Waals Forces: A Handbook for Biologist, Chemists, Engineers, and Physicists*, Cambridge Univeristy Press, New York **2006**.

(16) C. B. Murray, C. R. Kagan and M. G. Bawendi, *Science*, 1995, **270**, 1335.

(17) S. M. Liff, N. Kumar and G. H. McKinley, *Nat. Mater.* 2007, **6**, 76.

(18) M. Es-Souni and H. Fischer-Brandies, *Adv. Funct. Mater.* 2008**, 18**, 3179.

(19) S.K. Smoukov, K.J.M. Bishop, B. Kowalczyk, A.M. Kalsin and B.A. Grzybowski, *J. Am. Chem. Soc.* 2007, **129**, 15623.

(20) K. V. Tretiakov, K. J. M. Bishop, B. Kowalczyk, A. Jaiswal, M. A. Poggi and B. A. Grzybowski, *J. Phys. Chem. A* 2009, **113**, 3799.

(21) S. Huda, S.K. Smoukov, H. Nakanishi, B. Kowalczyk, K. J.M. Bishop and B.A. Grzybowski, *Adv. Mater. Interfaces* 2010, **2**, 1206.

(22) M. G. Song, K. J. M. Bishop, A. O. Pinchuk, B. Kowalczyk and B. A. Grzybowski, *J. Phys. Chem. C*, 2010, **114**, 8800.

(23) B. Kowalczyk, I. lagzi, K.J.M. Bishop, D. Wang and B.A. Grzybowski *Nat.Mater.* 2012, **11**, 227.

(24) (a) N. Kubota, H. Otosaka, N. Doki, M. Yokota and A. Sato, *J. Cryst. Growth* 2000, **220**, 135; (b) S. Mann, J.M. Didymus, N.P. Sanderson, B.R. Heywood and E.J.A. Samper, *J. Chem. Soc. Farad. Trans.* 1990, **86**, 1873; (c) S.Y. Jing et al., *Mater. Lett.* 2007, **61**, 2281; (d) M. Oner and E. Akyol, *J. Cryst. Growth* 2007, **307**, 137; (e) J.H. Yang, L.M. Qi, D.B. Zhang, J.M. Ma and H.M. Cheng, *Cryst. Growth Des.* 2004, **4**, 1371; (f) J. Aizenberg, A.J. Black and G.M. Whitesides, *Nature* 1999, **398**, 495; (g) Y. Yeh and R.E. Feeney, *Chem. Rev.* 1996, **96**, 601; (h) L. Addadi and S. Weiner, *Angew. Chem. Int. Edit.* 1992, **31**, 153.

(25) (a) A.M. Kalsin, M. Fialkowski, M. Paszewski, S.K. Smoukov, K. J.M. Bishop and B.A. Grzybowski, *Science* 2006, **312**, 420. (b) A.M. Kalsin and B.A. Grzybowski, *Nano Lett.* 2007, **7,** 1018.

(26) K.J.M. Bishop, N.R., Chevalier and B.A. Grzybowski, *J. Phys. Chem. Lett.* 2013, **4**, 1507.

(27) B. Kowalczyk, D.A. Walker, S. Soh and B.A. Grzybowski, *Angew. Chem. Int. Ed.* 2010, **49,** 5737.

(28) L. J. Sherry, R. C. Jin, C. A. Mirkin, G. C. Schatz and R. P. Van Duyne, *Nano Letters* 2006, **6**, 2060.

(29) A. J. Haes and R. P. Van Duyne, *J. Am. Chem. Soc.* 2002, **124**, 10596.

(30) D. A. Walker, K. P. Browne, B. Kowalczyk and B. A. Grzybowski, *Angew. Chem. Int. Edit.* 2010, **49**, 6760.

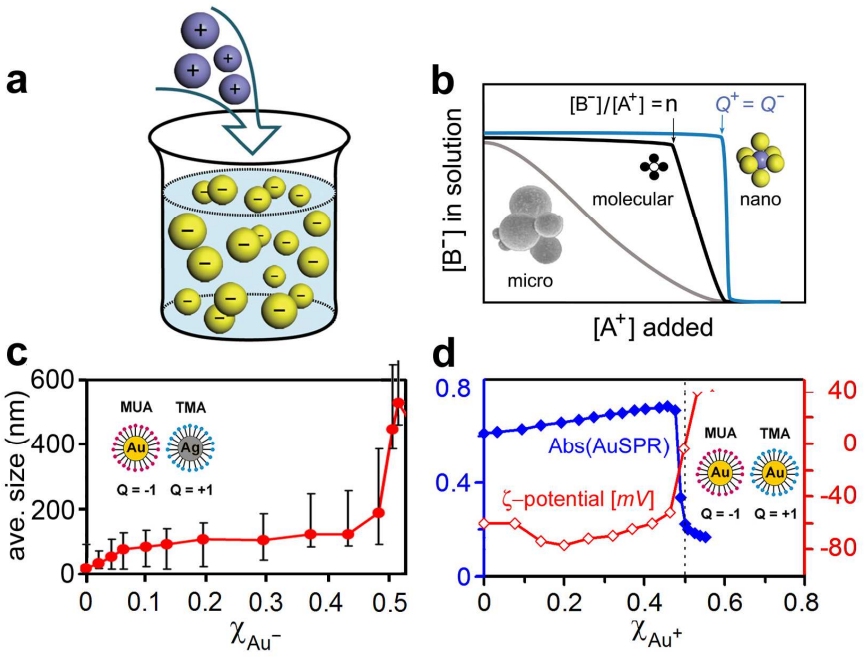

Figure 1. Precipitation of oppositely charged NPs at the point of electroneutrality. a) Scheme of the titration experiment in which a solution of negatively charged NPs (e.g., Au/SH-$(CH_2)_{11}$-COO^-, *yellow*) is titrated with a solution containing positively charged NPs (e.g., Ag/SH-$(CH_2)_{11}$-$N(CH_3)_3^+$; blue-gray). **b)** The titrated nanoparticles precipitate from solution only upon reaching the point of NP charge neutrality. This behavior is distinct from that of molecular ions, which usually precipitate at a threshold K_{sp} value, and is in sharp contrast to continuous precipitation of charged microparticles. **c)** Average size of aggregates measured by DLS during titration of 11 nm AuMUAs with 11 nm AgTMAs. **d)** Intensity of the Au SPR band at λ_{max} 520-550 nm (blue line) and the values of the ζ-potential (red line) for the titrations of oppositely charged, 5.5 nm AuNPs. In c) and d), the solutions of each type of NPs were 2 mM in terms of the metal atoms. Reproduced from ref 10.

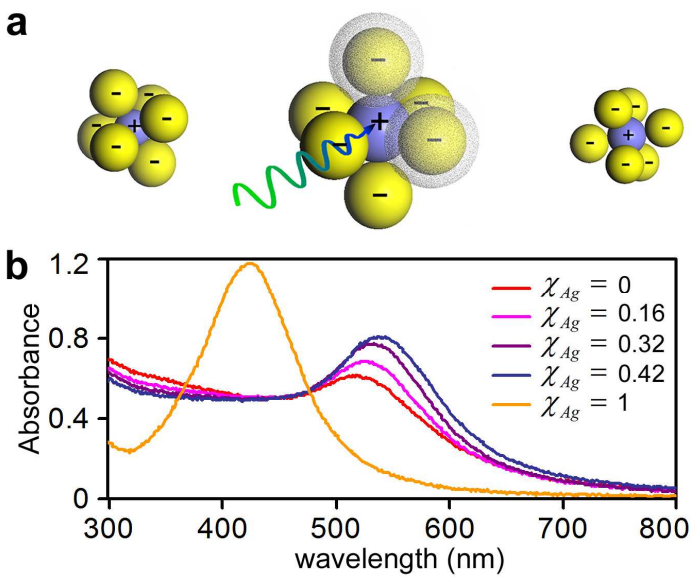

Figure 2. Complex-like structures forming by self-assembly of oppositely charged NPs. a) Qualitative scheme of charged core-and-shell aggregates forming from NPs of opposite polarities (*yellow* = AuNPs, *blue* = AgNPs) at the early stages of a titration. The halos in the middle structure illustrate the ionic atmospheres that screen electrostatic repulsions between like-charged shell NPs. For details, see refs 5 and 10. **b)** UV-Vis spectra for the titration of 5.5 nm AuMUAs with 6.5 nm AgTMAs. The legend gives the number of AgNP equivalents added; the spectrum of pure AgTMAs (orange line, $\chi_{Ag} = 1$) is included for reference. Note that all the way up to the titration point, the SPR band of silver at 424 nm is absent, while that of gold gradually increases. Reproduced from ref 10.

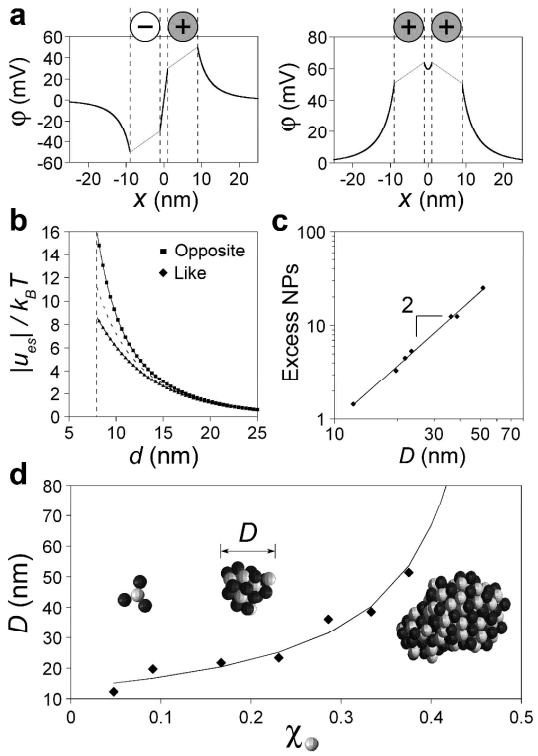

Figure 3. Electrostatic potentials between charged nanoparticles. a) Electrostatic potential along the axis, *x*, connecting two oppositely charged (*left*) and like charged (*right*) NPs. Note that the potential is smaller between oppositely-charged NPs, resulting in desorption of counterions and enhanced electrostatic attraction. **b)** Magnitude of the electrostatic interaction energy, $|u_{es}|$, between two oppositely charged and two like-charged NPs as a function of the distance between their centers, *d*, and in units of k_BT. The dashed line is the approximate form $u_{es}(d) = 4\pi\varepsilon_0\varepsilon\varphi_s^2 R^2 \exp[-\kappa(d-2R_1)]/d$. **c)** Results of MC simulation indicate that the average number of excess NPs per cluster increases quadratically with cluster diameter. Note that both *x* and *y* scales are logarithmic. **d)** MC simulations predict that the mean diameter, *D*, of clusters composed of equally-sized NPs (here, 6 nm metal core) increases with the fraction of "minority"

NPs in solution. The line gives the $D \sim (0.5 - \chi)^{-1}$ fit which diverges at $\chi = 0.5$. Reproduced from ref 10c.

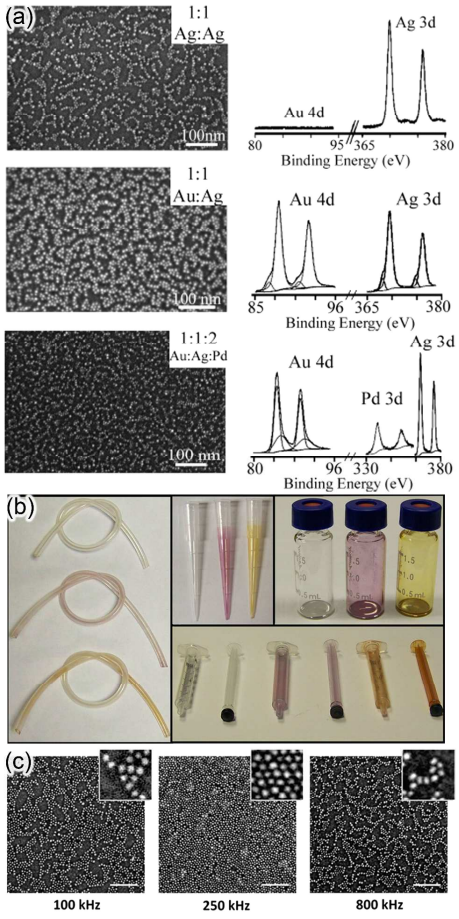

Figure 4. Formation of NP coatings from oppositely charged NPs. a) SEM images (*left panel*) and XPS spectra showing structure and metal composition (*right panel*) of coatings composed of oppositely charged NPs having same or different metal cores: AgMUA/AgTMA (top), AuMUA/AgTMA (middle) and AuTMA/AgTMA/PdMUA (bottom). TMA = SH-$(CH_2)_{11}$-$N(CH_3)_3^+$; MUA = SH-$(CH_2)_{11}$-COO^-. **b)** Examples of medically relevant components coated with bacteriostatic NP monolayers of oppositely charged nanoparticles: Tygon-R tubing, polypropylene micropipette tips, glass vials, and polypropylene syringes. Yellow-orange coatings are made of AgMUA/AgTMA; pink coatings, from AuMUA/AgTMA. Uncolored pieces are shown for reference. **(c)** SEM images of typical binary AuMUA/AgTMA NPs

coatings deposited with different AC frequencies ranging from 100 to 800 kHz. All samples were prepared at the same electric field strength of 150 V cm^{-1} (i.e., 5 V across 340 μm) and 15 min of field application. Scale bars are 100 nm; the insets are 50 nm × 50 nm. Adapted from refs 19, 21, and 22.

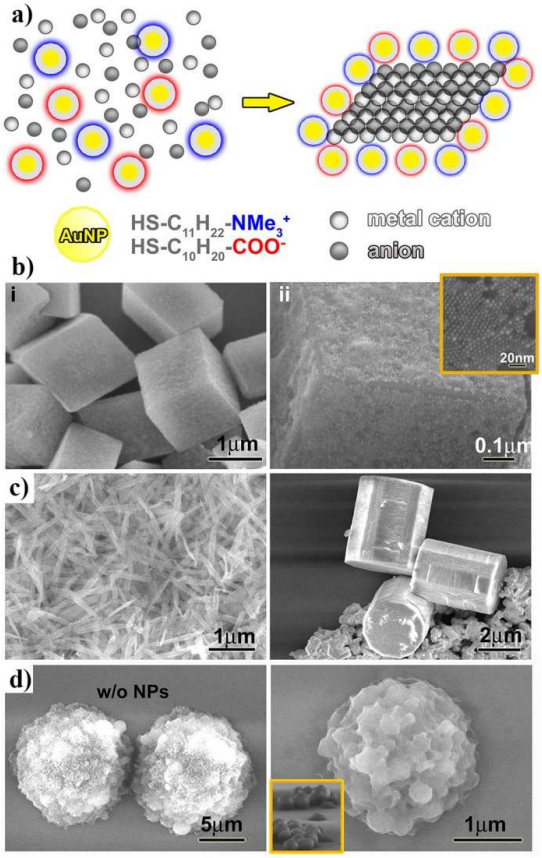

Figure 5. NP surfactants control the growth of inorganic salt microcrystals. The scheme in **(a)** illustrates the process of crystal growth. When the salt starts to crystallize, NPs adsorb onto the crystal's faces thereby slowing its growth. **(b)** Shows SEM images – at two different magnifications – of calcite microcrystals coated with NP monolayers. The right image illustrates that the NP coating is sparser near the microcrystal's edges. The inset zooms on the regularly packed domains within the NP monolayer. **(c)** Two further examples of NP-coated microcrystals (*left*) $Cu(OH)_2$ and (*right*) K_2SO_4. **(d)** SEM images of (L)-lysine microcrystals grown in the absence (*left*) and in the presence (*right*) of Au NPs (C_{NP} = 0.8 mM, C_{lysine} = 3 mM). For images zooming on the individual NPs and for more examples of coated microcrystals, please see ref 23 from which the figure has been adapted.

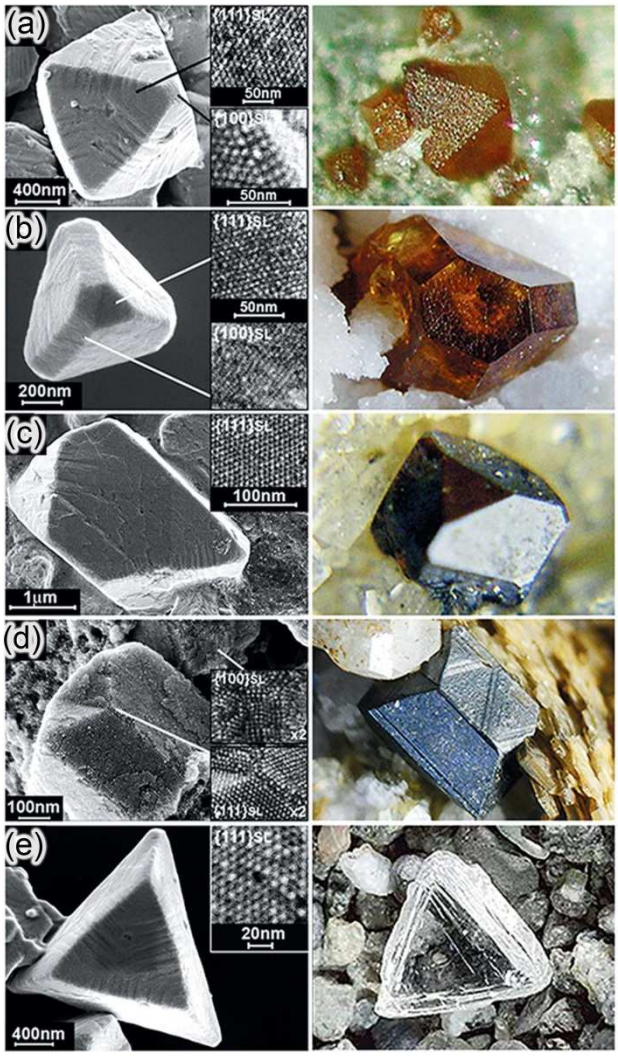

Figure 6. Diamond-like NP crystals. The left column has the SEM images of diamond-like crystals formed from oppositely charged, 5 nm Au and AgNPs. Insets zoom on the particles on the crystals' faces. The right column has the zinc-blend crystals (lattice isostructural with diamond) with similar morphologies. See [25a] for details.

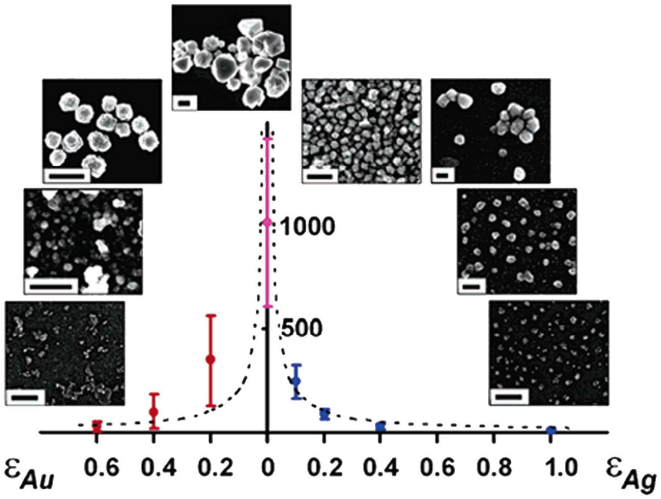

Figure 7. Controlling the size of NP crystals. Size control during crystallization of equally sized, ~ 5 nm AuMUA and AgTMA nanoparticles at pH 10. The graph plots average sizes (in nm) of crystals grown with different amounts of excess gold or silver NPs ($\varepsilon_{Au}/\varepsilon_{Ag}$, respectively). Vertical bars denote the ranges of the crystal sizes observed; insets have the SEM images of typical crystals (scale bars are 100 nm for $\varepsilon_{Au} = 0.6$ and $\varepsilon_{Ag} = 0.2$, 0.4, 1.0, and 1 μm for all other experiments). Dashed line is a theoretical fit to the expected $d \propto 1/\varepsilon_{Ag}$ dependence. Reproduced from ref 25b.

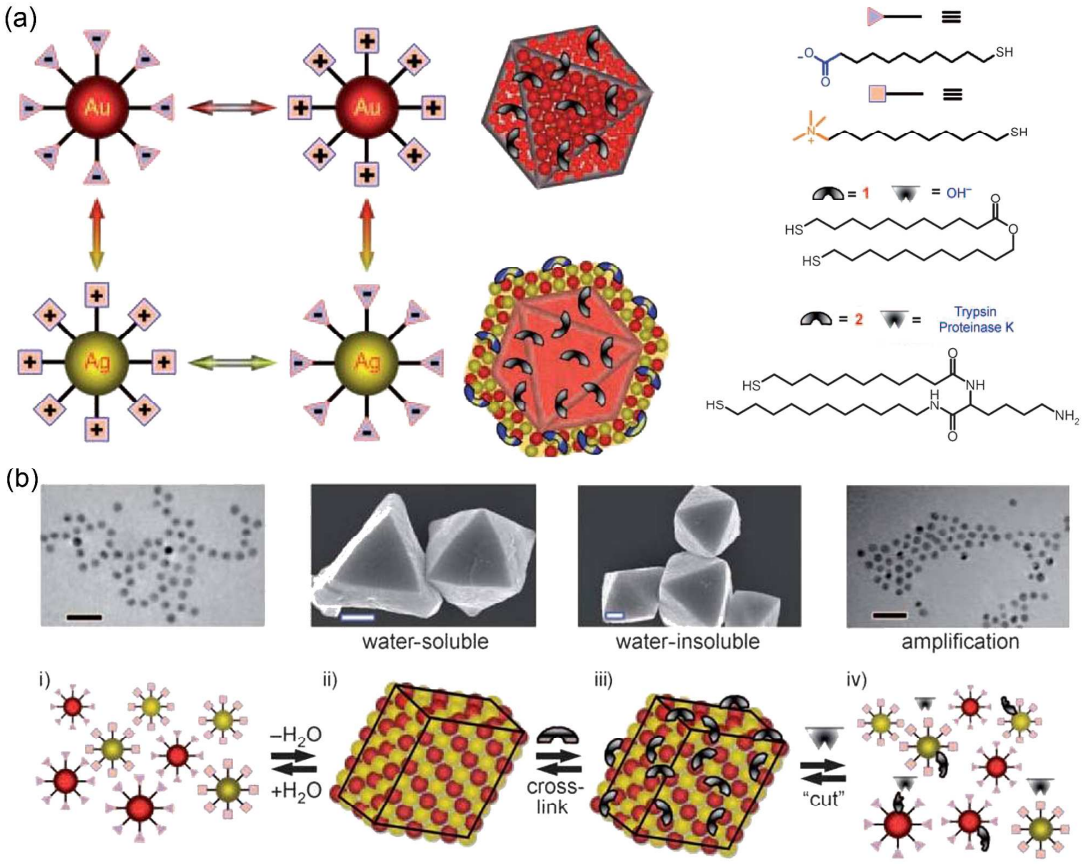

Figure 8. Nanoparticle crystals and core-and-shell ("Russian doll") crystals. a) Scheme of nanoparticles, crystals, and core-shell ("Russian Doll") crystals used for amplified sensing. The structures on the right are thiols used for coating the nanoionic NPs, and also of two dithiols used to crosslink the crystals. One of the dithiols shown can be "cut" by hydroxyl ions; the other is cut by enzymes such as Trypsin or Proteinase K. **b)** Procedure of amplified chemical sensing using nanoparticle supracrystals. Crystals self-assemble from oppositely charged NPs *(i)* and are soluble in water *(ii)*. These crystals gain permanence and become water-insoluble when they are cross-linked with dithiols containing cleavable groups (see examples in a) *(iii)*. When a specific

analyte is added, the cross-links are chemically cut, and the crystals disintegrate into individual nanoparticles *(iv)*. Reproduced from reference 27.

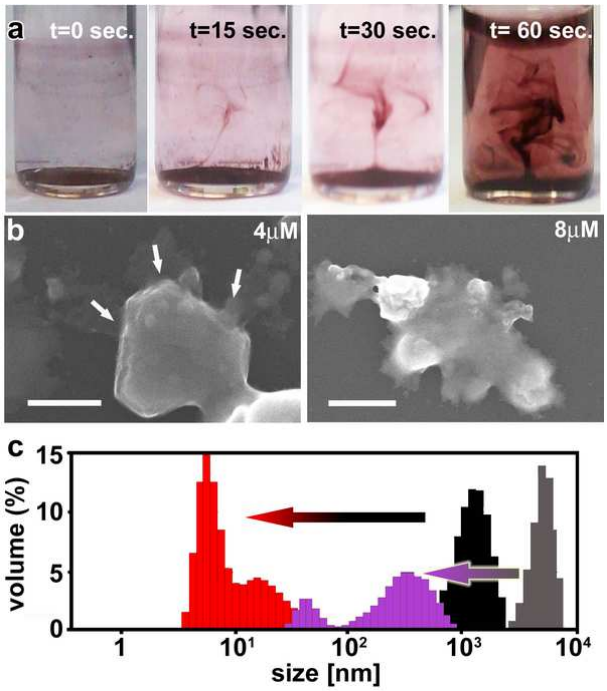

Figure 9. Dissolution of the dithiol-crosslinked NP crystals. a) Optical images illustrating dissolution of the crystals (here, crosslinked with **1** from Figure 8) upon addition of 5 μL of 10 mM $(CH_3)_4N^+OH^-$ base. **b)** Gradual dissolution of the crystals from (a) monitored using SEM. The concentrations of the base added are indicated in the upper-right corners of the images. The hazy regions around the crystal in the left image (indicated by white arrows) correspond to individual NPs "spilling out". Scale bars = 1 μm. **c)** Particle size distributions recorded by DLS. Black histogram – undissolved NP crystals crosslinked with **1**; Red histogram – particles from the dissolution of the crystals (upon addition of 10 μL of 10 mM $(CH_3)_4N^+OH^-$); Gray histogram – crosslinked, disordered NPs (crosslinker **1** in Figure 8); Violet histogram – aggregates from the dissolution of the disordered aggregates (after 24 hrs; cutting agent: 10 μL of 50 mM $(CH_3)_4N^+OH$). Reproduced from reference 27.

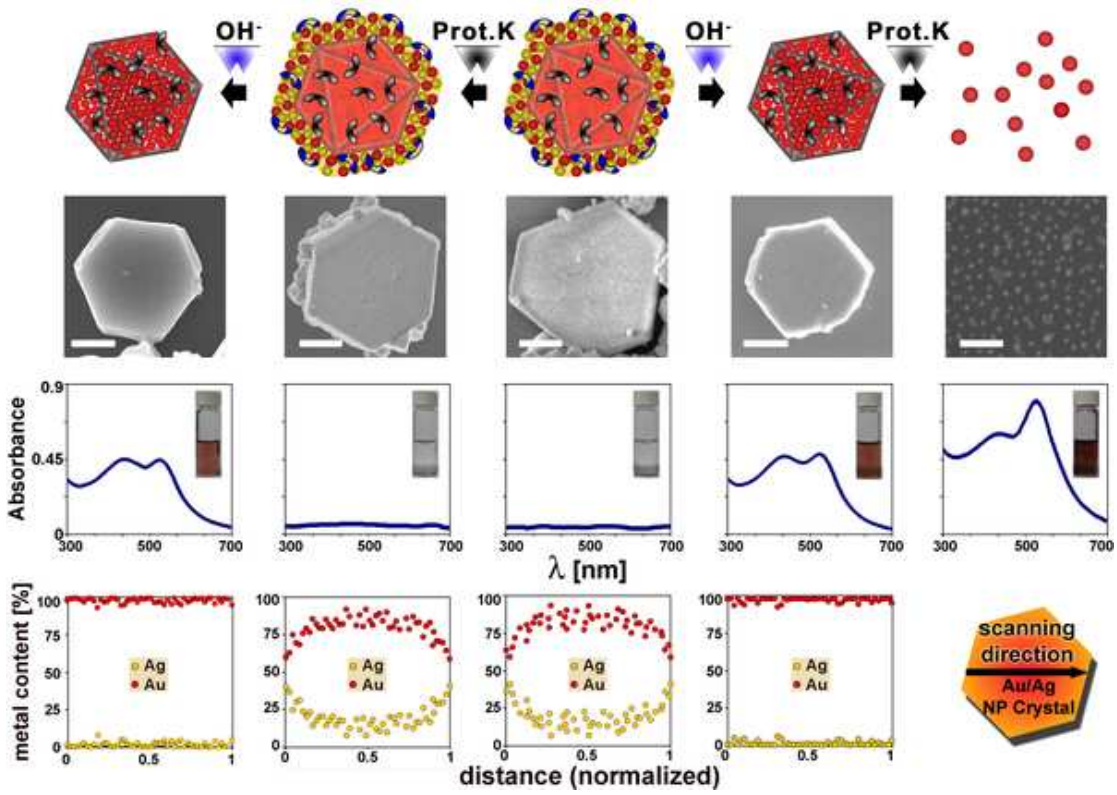

Figure 10. Sensing by core-and-shell crystals. When the core-and-shell crystals (*middle column*) are exposed first to the solution of an analyte cutting the outer crosslinks (here OH^- cutting **1** from Figure 8) and are then transferred into the solution containing analytes cutting the inner crosslinks (here proteinase K cutting **2**), both the core and the shell dissolve completely into individual NPs (*rightmost column*). When, however, the crystals are first exposed to the enzyme and only then to the base, only the shell dissolves leaving behind intact crystal "cores" (*leftmost column*). The specific crystals used here had the cores composed of AuTMA and AuMUA NPs and shells made of AgTMA and AuMUA NPs. The second row from the top shows typical SEM images of the crystals (scale bars = 500 nm; 100 nm in the rightmost image). The third row shows the UV-Vis spectra and optical images of the solutions. Solutions are clear

if crystals are not dissolved, orange if only the shells are dissolved, and dark red if both the shells and the cores are dissolved. The bottom row has typical EDS composition scans across individual crystals. Intact core-and-shell crystals contain χ_{Au}~78% Au and χ_{Ag}~22% Ag (composition averaged over scan length); when the shell is dissolved, the composition of the core is pure Au. Reproduced from reference 27.

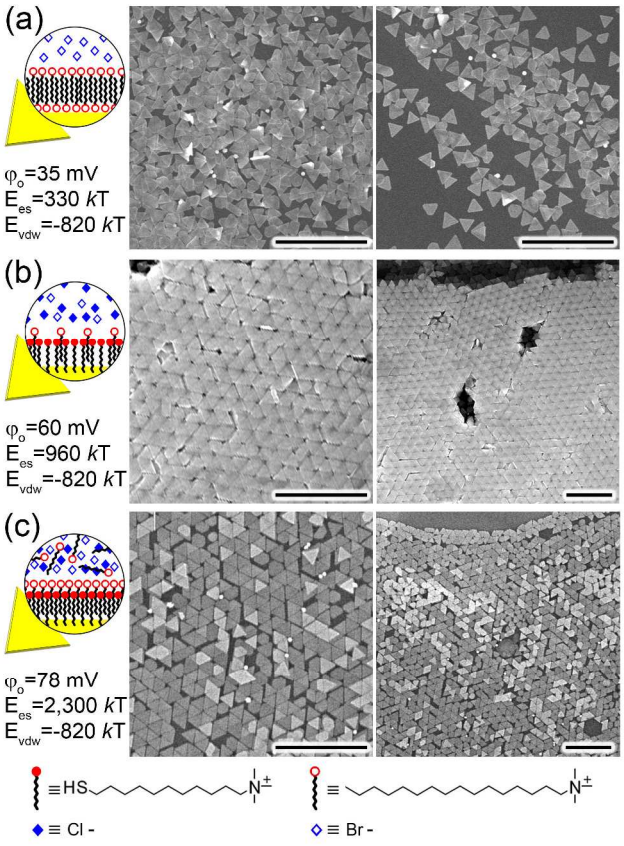

Figure 11. Self-assembly of nanotriangle lattices facilitated by repulsive electrostatic interactions. a) Gold nanotriangles, AuNTs, stabilized only by excess cetyltrimethylammonium bromide (CTAB) surfactant (20 mM CTAB, surface potential φ_o = 35 mV, E_{el} ~ 330 kT) form disordered aggregates. **b)** Triangles functionalized with positively charged SAMs (here, of TMA thiols) and with only small quantities of CTAB surfactant present (< 1 mM CTAB, φ_o = 60 mV, E_{el} ~ 960 kT) organize into large, ordered crystals. **c)** AuNTs stabilized with TMA SAMs and in the presence of excess CTAB (20mM CTAB, φ_o = 79 mV, E_{el} ~ 2,300 kT) give large monolayer arrays. All scale bars = 1 μm.

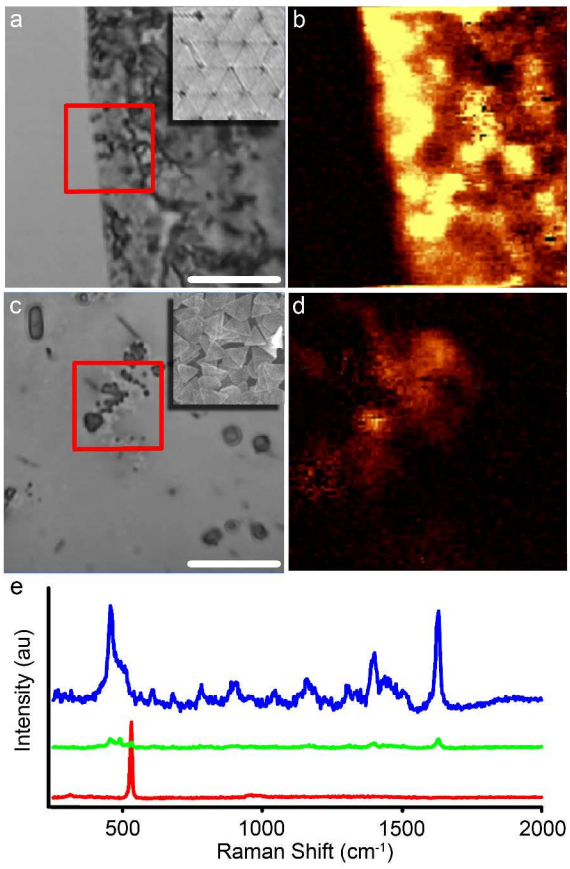

Figure 12. SERS sensing using nanotriangle lattices. a) Optical image (a) and confocal Raman mapping (b) of ordered NT crystals. The inset in (a) is representative SEM image of ordered NT array and the red box defines the region over which the Raman map, (b), was collected. Optical image (c) and confocal Raman mapping (d) of randomly assembled NT aggregates. The inset in (c) is a representative SEM image of the orderless NT aggregates and the red box defines the region over which the Raman map, (d), was collected. Scale bars in optical images are 10 µm. Both Raman maps are 10 µm by 10 µm (100 by 100 pixels); each pixel is the integration of the MB peak located at ~1620 cm^{-1}. (e) The Raman spectra collected for MB on an ordered NT crystal (blue spectrum; 1 sec integration time) shows enhancement an order of magnitude larger

than enhancement of MB peaks by disordered NT aggregates (green spectrum; 1 sec integration time). In the absence of NTs, there is no enhancement of the MB peaks (red spectrum; 30 sec integration time) and only Si peak (from the substrate) is observed (~600 cm^{-1}). Each spectrum has been baseline-corrected and off-set for clarity.